Journal of
Computational and Theoretical Nanoscience
Vol. 4, 84–95, 2007

Fast Bessel Matching

Julio A. Kovacs[1,*], Ruben Abagyan[1], and Mark Yeager[2,3]

[1] *Department of Molecular Biology and* [2] *Department of Cell Biology,*
The Scripps Research Institute, La Jolla, CA 92037, USA
[3] *Division of Cardiovascular Diseases, Scripps Clinic, La Jolla, CA 92037, USA*

A key step in 3D single particle reconstruction, is the 2D image alignment kernel, which largely determines the efficiency and accuracy of the overall reconstruction procedure. In this work we present *Fast Bessel Matching* (FBM), a real-space, correlation-based approach to perform the 2D alignment step. By casting the matching problem into a formulation involving three angular parameters, the problem is reduced to the calculation of a single 3D fast Fourier transform. An extra speedup is accomplished by rapidly decaying factors in the formula for the correlation transform. We also consider variations of the RPC ("resampling to polar coordinates") and the FRM2D ("fast rotational matching in 2D") methods, including a radially dependent angular sampling. We perform the operation counts for these variations and for FBM, observing that FBM is more than 2 times faster than any of the others. We also note that the Fourier-space SCF (self-correlation function) method has, for usual values of the sampling parameters, an operation count comparable to that of FBM. Finally, we argue that FBM might be the optimal real-space correlation-based image-matching method in such applications as EM image reconstruction. This paper deals exclusively with the theory of our approach; implementation and applications will be presented elsewhere.

Keywords: Image Reconstruction, Matching, Alignment, Bessel Function, Fourier–Bessel Transform.

1. INTRODUCTION

The computational problem of matching—bringing into register—two given objects appears in a wide variety of scientific fields, such as pattern recognition, image processing, engineering, machine vision, biophysics, biomedical imaging, etc. In this paper, we concentrate on the matching of 2-dimensional (2D) images, specifically those encountered in the reconstruction process of 3D electron-microscopy (EM) maps by the single particle technique, where the usually high noise level precludes an accurate determination of the centers of mass of the images, and thus makes it necessary to perform a joint search of the motion's parameters. However, our method is of general applicability to other disciplines as well.

In recent years, increasingly sophisticated and powerful techniques in single particle analysis have produced a wealth of low- to medium-resolution reconstructions.[1] The two key steps in single particle analysis—2D classification and 3D refinement—require a computationally expensive alignment of a set of particle images with a set of reference images.[2] The number of particle images necessary to achieve resolutions of 4 Å or better in cryo-EM is of the order of 10^6 (Ref. [3]). Consequently, the efficiency of the alignment kernel is a limiting factor in improving the resolution.

Various 2D alignment methods are in common use. They are well described elsewhere.[2] In addition, a more recent approach, FRM2D ("fast rotational matching in 2D"), has been proposed.[4] Methods such as SCF (self-correlation function), which operate in Fourier space by using the amplitudes (moduli of the Fourier transforms), can decouple the rotational and translational searches,[5,6] making them of lower order of complexity than real-space methods. Although more efficient than real space methods, they are less robust in the analysis of images with low signal-to-noise ratio (SNR), due to the loss of information that occurs by not considering the phases of the Fourier transforms.

In this article, we describe a real-space alignment method based on maximizing the cross-correlation function. Our method relies on a factorization of motions in the plane (which is analogous to that used in the FRM (Fast Rotational Matching) method on the sphere)[7] and on combining this with key properties of Bessel functions, allowing us to obtain a formula for the Fourier transform of the correlation function in terms of the Fourier–Bessel transforms of the two images. Hence, we call this

*Author to whom correspondence should be addressed.

 1546-198X/2007/4/084/012 doi:10.1166/jctn.2007.007

method *Fast Bessel Matching* (FBM). In this work we present the theoretical development of this approach; a future publication will deal with benchmarking and applications to EM reconstructions.

The use of Fourier and Bessel expansions in biological applications has been very fruitful, and it would be difficult to give a complete bibliography on this subject. But let us just mention a few important applications. Fourier methods have been used as the basic tool to efficiently compute correlations and convolutions, which have been used, among other applications, for fitting of molecular models into experimental EM maps[10] and for molecular docking.[11] Bessel transforms have been used, for instance, in the reconstruction of helical structures (Wang and Nogales[12] and references therein) and in the estimation of alignment errors in sets of 2D images.[13] However, to our knowledge, the present work is the first one in making use of the special properties of Bessel functions to derive a fast image-matching algorithm.

Of particular relevance here, as to both the overall goal and the mathematical foundation, is the work of Navaza[9] in which he presents a model-free reconstruction method based on an elegant calculation of the Fourier–Bessel transforms of projection images in terms of the spherical harmonic coefficients of the Fourier transform of the 3D scattering density.

In addition, we make variations of the standard angular sampling in the RPC (resampling to polar coordinates) and FRM2D methods, to effectively make it radially dependent, in fact proportional to the radius. This is related to the basic idea in the original implementation of the RPC method[14] to avoid oversampling near the center. Also, we note that, by a change of variables, it is possible to reduce the bandwidth for one of the parameters in FRM2D, bringing it to a complexity level similar to that of RPC. These optimizations significantly reduce the operation counts of both methods. FBM shows an operation count of less than half of those of the optimized RPC or FRM2D methods. Also, we note that the Fourier-space SCF method has an operation count that is comparable to that of FBM for commonly used values of the sampling parameters.

2. METHODS

2.1. Continuum Theory

When matching a reference image with a particle image, the center of mass (COM) of the former can be accurately computed, while that of the latter might be several pixels off due to the high level of noise present in the image. Let $\rho_{\max}$ denote the maximum expected value (in pixels) of this offset. In other words, $\rho_{\max}$ is an upper bound of the error in the calculation of the COM of the particle images. We estimate this error bound as 2.5% of the image size $2A$ (A being its radius) for cases of high SNR, and as 5% of $2A$ for cases of low SNR.

2.1.1. Preliminary Formulas

Consider a motion $M\colon \mathbb{R}^2 \to \mathbb{R}^2$ of the plane. We can represent M by a sequence of operations: a rotation of angle ψ around the origin, a translation of length ρ along the x axis, and finally a rotation of angle ϕ around the origin. Equivalently, this can be expressed as a rotation of angle $\phi+\psi$ around the origin followed by a translation of length ρ in the direction forming an angle ϕ with the x axis:

$$M = R_\phi \circ T_{(\rho,0)} \circ R_\psi = T_{(\rho\cos\phi,\,\rho\sin\phi)} \circ R_{\phi+\psi} \tag{1}$$

We represent this motion by the triplet (ϕ, ρ, ψ).

Now, let p and p' be two points related by $M(p') = p$, and let (r, λ) and (r', λ') be the polar coordinates of p and p', respectively. According to the formula for M, we have:

$$p = T_{(\rho\cos\phi,\,\rho\sin\phi)}(R_{\phi+\psi}(p')) \tag{2}$$

Considering p and p' as complex numbers, $p = re^{i\lambda}$, $p' = r'e^{i\lambda'}$, this equation can be written as:

$$r'e^{i\lambda'} = (re^{i\lambda} - \rho e^{i\phi})e^{-i(\phi+\psi)} \tag{3}$$

Let J_n denote the Bessel function of the first kind of order n. In the above situation, the addition formula for Bessel functions given in Watson[15] (p. 360) can be rewritten, using the substitution $Z = rx$, $z = \rho x$, $\varpi = r'x$, and transposing some factors, as:

$$J_m(r'x)e^{im\lambda'} = \sum_{n=-\infty}^{\infty} J_n(rx)J_{n-m}(\rho x)e^{i[n(\lambda-\phi)-m\psi]} \tag{4}$$

where x is any non-negative real number.

Consider now two motions, $M_i(\phi_i, \rho_i, \psi_i)$, $i = 1, 2$, and their composition $M = M_1 \circ M_2$. The parameters of M are readily obtained by working, as before, with complex numbers. We have $M_2(p) = e^{i\phi_2}(\rho_2 + e^{i\psi_2}p)$, and therefore:

$$\begin{aligned} M_1(M_2(p)) &= e^{i\phi_1}\left(\rho_1 + e^{i\psi_1}e^{i\phi_2}(\rho_2 + e^{i\psi_2}p)\right) \\ &= \rho_1 e^{i\phi_1} + \rho_2 e^{i(\phi_1+\phi_2+\psi_1)} + e^{i(\phi_1+\phi_2+\psi_1+\psi_2)}p \end{aligned} \tag{5}$$

Hence,

$$\rho = |\rho_1 + \rho_2 e^{i(\phi_2+\psi_1)}| = \sqrt{\rho_1^2 + \rho_2^2 + 2\rho_1\rho_2\cos(\phi_2+\psi_1)} \tag{6}$$

$$\phi + \psi = \phi_1 + \phi_2 + \psi_1 + \psi_2 \tag{7}$$

Therefore, we can apply the composition formula for Bessel functions (Vilenkin,[16] p. 209, Eq. (3)) to our triangle with sides $\rho_1 x$, $\rho_2 x$, and ρx. We get:

$$e^{in(\phi-\phi_1)}J_n(\rho x) = \sum_{k=-\infty}^{\infty} e^{ik(\phi_2+\psi_1)}J_{n-k}(\rho_1 x)J_k(\rho_2 x) \tag{8}$$

After some rearrangements, this formula can be written in the following convenient way for later use:

$$\begin{aligned} e^{i(n\phi+m\psi)}J_{n-m}(\rho x) = \sum_{h=-\infty}^{\infty} & e^{i(n\phi_1+h(\phi_2+\psi_1)+m\psi_2)} \\ & \times J_{n-h}(\rho_1 x)J_{h-m}(\rho_2 x) \end{aligned} \tag{9}$$

2.1.2. Fourier–Bessel Transform

Given a function $f: \mathbb{R}^2 \to \mathbb{R}$, its *Fourier–Bessel transform* is defined as the following family of functions (Vilenkin,[16] p. 219), defined for $x \geq 0$:

$$F_m(x) = \int_0^\infty \hat{f}_m(u) J_m(ux) u du \tag{10}$$

where $\hat{f}_m(u)$ is the Fourier transform of f along the polar angle for a fixed radius u:

$$\hat{f}_m(u) = \frac{1}{2\pi} \int_0^{2\pi} f(u, \theta) e^{-im\theta} d\theta \tag{11}$$

We note that what is usually called "Fourier–Bessel transform" is just the Bessel transformation given by Eq. (10), with no previous Fourier transformation.

The Fourier transform can be recovered from $F_m(x)$ thus:

$$\hat{f}_m(u) = \int_0^\infty F_m(x) J_m(ux) x dx \tag{12}$$

and therefore the original function f can be expressed as:

$$\begin{aligned} f(r, \lambda) &= \sum_{m=-\infty}^{\infty} \hat{f}_m(r) e^{im\lambda} \\ &= \sum_{m=-\infty}^{\infty} e^{im\lambda} \int_0^\infty F_m(x) J_m(rx) x dx \end{aligned} \tag{13}$$

2.1.3. Fundamental Correlation Formula

Let $f: \mathbb{R}^2 \to \mathbb{R}$ and $g: \mathbb{R}^2 \to \mathbb{R}$ be two images that we want to match. For a given motion $M: \mathbb{R}^2 \to \mathbb{R}^2$ with parameters (ϕ, ρ, ψ), let Λ_M denote the *motion operator*, which, applied to an image, gives the moved image, namely:

$$\Lambda_M(g) = g \circ M^{-1} \tag{14}$$

As before, for any point p on the plane, let $p' = M^{-1}(p)$, and let us denote by (r, λ) and (r', λ') their respective polar coordinates. Then, by Eq. (13),

$$\Lambda_M(g)(p) = g(p') = \sum_m e^{im\lambda'} \int_0^\infty G_m(x) J_m(r'x) x dx \tag{15}$$

where $G_m(x)$ is the Fourier–Bessel transform of g. By using the addition formula, Eq. (4), we get, after some rearrangements:

$$\begin{aligned} \Lambda_M(g)(p) = \sum_n e^{in\lambda} \int_0^\infty \left(\sum_m G_m(x) J_{n-m}(\rho x) e^{-i(n\phi + m\psi)} \right) \\ \times J_n(rx) x dx \end{aligned} \tag{16}$$

from which we can read off the Fourier–Bessel transform of $\Lambda_M(g)$, denoted here by G^M:

$$(G^M)_n(x) = \sum_m G_m(x) J_{n-m}(\rho x) e^{-i(n\phi + m\psi)} \tag{17}$$

Now we can compute the correlation function between f and the moved g, starting by using their Fourier expansions $f(r, \lambda) = \sum_m e^{im\lambda} \hat{f}_m(r)$ and $\Lambda_M(g)(r, \lambda) = \sum_n e^{in\lambda} \widehat{\Lambda_M(g)}_n(r)$:

$$\begin{aligned} c(M) &= \int_{\mathbb{R}^2} f \cdot \Lambda_M(g) \\ &= \int_0^\infty \int_0^{2\pi} f(r, \lambda) \overline{\Lambda_M(g)(r, \lambda)} r d\lambda \, dr \\ &= 2\pi \sum_m \int_0^\infty \hat{f}_m(r) \overline{\widehat{\Lambda_M(g)}_m(r)} r dr \end{aligned} \tag{18}$$

which, due to Plancherel's theorem for Fourier–Bessel transforms (Vilenkin,[16] p. 218), is equal to:

$$2\pi \sum_m \int_0^\infty F_m(x) \overline{(G^M)_m(x)} x dx \tag{19}$$

Substituting Eq. (17) we get:

$$c(M) = 2\pi \sum_{m, m'} e^{i(m\phi + m'\psi)} \int_0^\infty F_m(x) \overline{G_{m'}(x)} J_{m-m'}(\rho x) x dx \tag{20}$$

We now factor the motion M as $M = M_1 \circ M_2$, as in Section 2.1.1, using the following parameters for M_1 and M_2:

$$\begin{aligned} \phi_1 &= \xi, & \rho_1 &= b, & \psi_1 &= 0 \\ \phi_2 &= \eta + \epsilon, & \rho_2 &= b, & \psi_2 &= \omega \end{aligned} \tag{21}$$

where $b = \rho_{\max}/2$, and ϵ is a small angle used to avoid duplication of radii in the sampling of η (see Section 2.2.3). Thus, the angles ξ, η, and ω parameterize the motion M, and are the ones to be searched in the maximization of $c(M)$. The meaning of these parameters is very concrete, as shown in Figure 1.

Using the composition formula, Eq. (9), with these parameters, in Eq. (20), we obtain:

$$\begin{aligned} c(M) = 2\pi \sum_{m, h, m'} e^{i(m\xi + h(\eta + \epsilon) + m'\omega)} \\ \times \int_0^\infty J_{m-h}(bx) J_{h-m'}(bx) F_m(x) \overline{G_{m'}(x)} x \, dx \end{aligned} \tag{22}$$

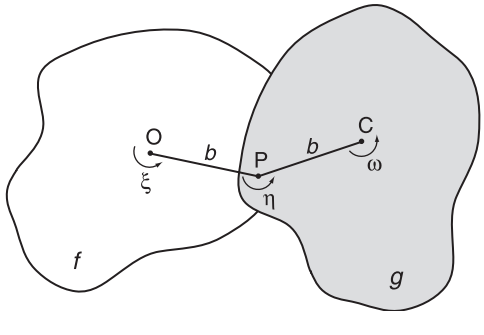

Fig. 1. Setup of our approach. The image f is fixed, while image g (to which point C is attached) moves according to the angles ξ, η, and ω. The arm length b is fixed at a (usually small) value that is chosen according to the estimated error in the determination of the centers of mass of the images. These approximate centers of mass are denoted by O and C.

Due to the behavior of Bessel functions:

$$J_n(x) \sim \frac{1}{\sqrt{2\pi n}}\left(\frac{ex}{2n}\right)^n \tag{23}$$

which holds for large n (Abramowitz and Stegun,[17] p. 365) or for small x (which results from combining Eq. (9.1.7) (p. 360 in Abramowitz and Stegun)[17] with Stirling's formula for the Gamma function), it is convenient, as will be seen below, to make the following change of indices and variables:

$$\begin{aligned} h &= h_1 + m' \\ m &= m_1 + h = m_1 + h_1 + m' \\ \eta' &= \xi + \eta \\ \omega' &= \xi + \eta + \omega \end{aligned} \tag{24}$$

Then, $c(M)$ becomes a function $T(\xi, \eta', \omega')$ whose Fourier transform, as read off Eq. (22), is:

$$\widehat{T}(m_1, h_1, m') = 2\pi e^{i(h_1+m')\epsilon} \times \int_0^\infty F_{m_1+h_1+m'}(x)\overline{G_{m'}(x)} \times J_{m_1}(bx)J_{h_1}(bx)x\,dx \tag{25}$$

This is the fundamental equation of this paper.

2.2. Discretization and Bandwidths

2.2.1. Basics

In the previous section, we considered general images defined on the whole plane. Here we will restrict ourselves to the practical case where the supports of the images are bounded, and denote with A their radii, in pixels. Let p_s be the prescribed (average) number of (linear) pixels per sampled point. These samples can be obtained, for example, by averaging a number of pixels around each point. In order to compute the Fourier–Bessel transforms of the images, we need to express and sample them in polar coordinates. To determine the number of angular intervals s, note that s intervals on the perimeter of the image correspond to $2\pi A$ pixels (see Fig. 2), so each interval at the periphery is $2\pi A/s$ pixels long, and thus it is $\pi A/s$ pixels long at mid-radius. This length is therefore p_s, the average number of pixels per sample; hence

$$s = \frac{\pi A}{p_s} \tag{26}$$

Therefore, there are $A/p_s = s/\pi$ samples along the radius A of the image. Let us call $B = s/2$. This is then the assumed "bandwidth" of the images, i.e., the Fourier transforms in Eq. (11) are to be computed using $2B$ angular samples, and only for $|m| < B$. (They are assumed to vanish for $|m| \geq B$.)

Also, the upper limit of integration in the equation defining the Fourier–Bessel transform, Eq. (10), becomes A, and the integral is to be computed using $2B/\pi$ intervals of length p_s.

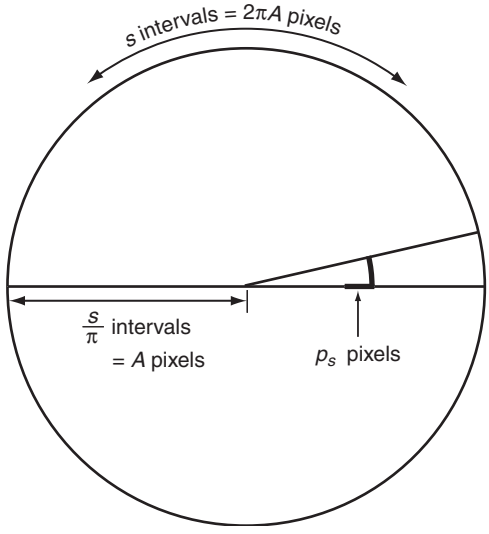

Fig. 2. Parameters using for sampling the images. The radius of the images is A pixels, and the prescribed average sampling interval is p_s pixels. This implies that s, the number of angular samplings, is $\pi A/p_s$, and there are s/π sampling intervals along the radius of the image.

2.2.2. Bandwidth for x

Next, we calculate the bandwidth for x, that is, the upper limit of integration in Eq. (25). We do this using Eq. (10) to determine the maximum x compatible with the number of samples along the radius, which is $2B/\pi$. According to the standard sampling theorem, this number of samples must be twice the highest frequency. This highest frequency is, more precisely, the number of cycles undergone by the oscillating function $J_m(ux)$ as u goes from 0 to A, and this must be multiplied by 2 to account for the fact that each u actually includes information (through $\hat{f}_m(u)$) from the whole circle of radius u, not only from a point at distance u from the origin. Now, $J_m(ux)$, as a function of u, behaves like $\sqrt{2/(\pi ux)}\cos(ux)$, modulo an m-dependent phase (Abramowitz and Stegun,[17] p. 364). Therefore, the number cycles for the highest x may be estimated as $x_{\max}A/(2\pi)$, and hence our equation for $x_{\max}$ is:

$$\frac{2B}{\pi} = 2 \cdot \frac{x_{\max}A}{2\pi} \cdot 2 \tag{27}$$

whence:

$$x_{\max} = \frac{B}{A} \tag{28}$$

Another, more rigorous, proof of this formula is given in Appendix A.

Next, we shall determine the bandwidths for ξ, η', and ω'.

2.2.3. Absolute Bandwidths

As to the samples for ξ and η, we note that the number of samples for ξ gives the number of angular samples of C,

while the number of samples for η gives the number of radial samples of C (see Fig. 1). Since the average distance between sampled points should be p_s, we see that $s_\xi = 2\pi b/p_s = \pi k$ and $s_\eta = k$, where

$$k = \frac{2b}{p_s} = \frac{\rho_{\max}}{p_s} \tag{29}$$

is the number of sampling points in which $\rho_{\max}$ is divided, which corresponds to the k of previous references.[2,4] Note that k values for η do produce k different radii (distances from O to C) if we take $\epsilon = \pi/(2k)$ in Eq. (21), since this value is 1/4 of the angular sampling step $2\pi/s_\eta$ (see Fig. 3). Since our original pair (ξ, η) was sampled with πk and k points, respectively, then the new pair $(\xi, \xi + \eta)$ will also be sampled using the same number of points (there is no change in the information content). Thus, $s_{\eta'} = k$. (As a matter of fact, we have the freedom to choose $s_\xi = ak$ and $s_{\eta'} = \pi k/a$, keeping their product constant. A more symmetric choice would be $a = \sqrt{\pi}$. Any of these gives an operation count of the same order, but different values of a produce different sampling patterns, which in principle could be adjusted according to specific needs or image features).

Finally, since $G_{m'}$ appears in Eq. (25) giving $\widehat{T}(m_1, h_1, m')$, and $G_{m'}$ is defined through Eq. (10) which contains $\hat{g}_{m'}$, and since the latter is assumed to vanish for $|m'| \geq B$ (i.e., the images are band-limited at B), we conclude that $|m'|$ has to be $<B$.

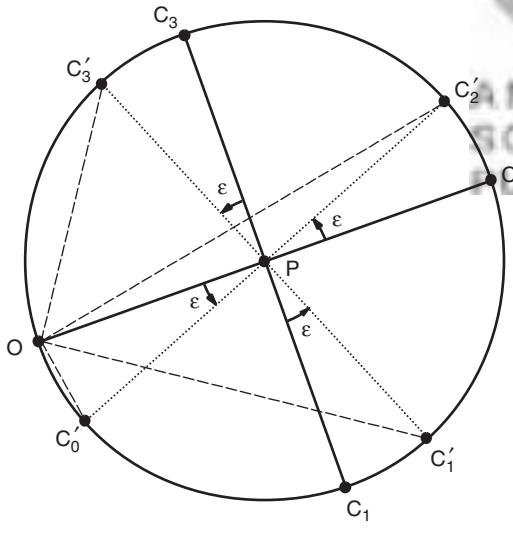

Fig. 3. This drawing describes how, by using the angle ϵ, the duplication of distances from O to the various centers is avoided. The points O, P, and Cs correspond to the points of the same names in Figure 1. The example shown corresponds to $s_\eta = k = 4$. If the ϵ rotation were not done, we would have duplication of distances: $\overline{OC_1} = \overline{OC_3}$, whereas by doing the rotation, the four distances $\overline{OC'_i}$, denoted by dashed lines, are all different. This is important in order to keep the number of η samples at k (number of radial samples) rather than $2k$.

To summarize:

$$|m_1| < \frac{1}{2}s_\xi = \frac{\pi k}{2} = \frac{2Bb}{A} \tag{30}$$

$$|h_1| < \frac{1}{2}s_{\eta'} = \frac{k}{2} = \frac{2Bb}{\pi A} \tag{31}$$

$$|m'| < B \tag{32}$$

where we used the relation $p_s = \pi A/(2B)$ and Eq. (29).

2.2.4. *x*-Dependent Bandwidths

Now we want to obtain bounds on m_1, h_1, and m' which depend on x, in order to use them in the numerical evaluation of $\widehat{T}$ using the fundamental Eq. (25). The idea is to evaluate the integrand for a series of values of x, and, for each value, determine the range of the indices, adding the evaluations to the corresponding entries of the array $\widehat{T}$. These bounds will also be used in the estimation of the operation count (Section 2.5).

The Bessel functions in the integral (25) drop quickly to 0 as their orders (m_1 or h_1) go beyond certain μ_0. Due to Eq. (23), we see that $\mu_0 \approx ebx/2$, since for n bigger than this value the quantity inside the parentheses in Eq. (23) (with x replaced by bx) gets <1, so its nth power will drop quickly. Therefore, we must have:

$$|m_1|,\ |h_1| \leq \frac{ebx}{2} \tag{33}$$

As pointed out above, the Fourier–Bessel transform, defined by Eq. (10) (with A as the upper integration limit), vanishes for $|m| \geq B$. We shall determine, for each x, a value $m_0(x)$ such that $F_m(x) \approx 0$ for $|m| > m_0$. (By what was just said, $m_0(x) \leq B$). First suppose x is small. Then, by Eq. (23), we have:

$$|J_m(rx)| \leq |J_m(Ax)| \approx \frac{1}{\sqrt{2\pi m}}\left(\frac{Aex}{2m}\right)^m \tag{34}$$

whence, by a similar argument as was used before, $m_0(x) \approx Aex/2$. Now let x be any value between 0 and B/A. First we notice that the lower limit of integration in Eq. (10) should be taken as $(A/B)|m|$, since, due to the band-limitedness of f, $\hat{f}_m(u) = 0$ for $|m| \geq (B/A)u$. Therefore, the integration interval has length $A(1-|m|/B)$, and so the relation $m_0(x) \approx Aex/2$, valid for small x, slows down as x (and m) increases. Although it is not possible to give an exact dependence of m_0 on x, the linear slowdown just obtained tells us that a parabolic relationship should be sufficiently accurate. So we model $m_0(x)$ as a parabola passing through the origin with slope $Ae/2$ and passing also through the point $(B/A, B)$. The equation of this parabola is:

$$m_0(x) = \frac{Ae}{2}x - \frac{A^2}{B}\left(\frac{e}{2} - 1\right)x^2 \tag{35}$$

Thus, in the integral (25) we must have $|m'| \leq m_0(x)$ and $|m_1 + h_1 + m'| \leq m_0(x)$ (however, the latter will not be used in the estimation of the operation count).

2.2.5. Discretization of the Integral (25)

The Fourier–Bessel transforms, Eq. (10), are computed using $2B/\pi$ intervals, since this is the number of samples over the radii of the images (Fig. 2). Therefore, the Fourier–Bessel transforms are also sampled in $2B/\pi$ intervals, of length

$$\Delta x = \frac{B/A}{2B/\pi} = \frac{\pi}{2A} \tag{36}$$

This is, then, the integration step to be used in the numerical evaluation of Eq. (25).

2.3. RPC Revisited

The RPC (Resampling to Polar Coordinates) method[2,4] consists in resampling one of the images (the static one) to polar coordinates with respect to selected origin locations of the other (moving) image. If f is the static image, its resampling to polar coordinates with respect to a center located at (a, b) is:

$$f^{(a,b)}(r,\beta) := f(a + r\cos\beta, b + r\sin\beta) \tag{37}$$

which we expand in Fourier series:

$$f^{(a,b)}(r,\beta) = \sum_m \big(\widehat{f^{(a,b)}}\big)_m(r) e^{im\beta} \tag{38}$$

The moving image g, rotated by an angle ϕ, is expanded in Fourier series as:

$$(\Lambda_\phi g)(r,\beta) = g(r,\beta-\phi) = \sum_m \hat{g}_m(r) e^{im(\beta-\phi)} \tag{39}$$

Then the correlation, as a function of the origin (a, b) and the rotation ϕ, is

$$\begin{aligned} c(\phi;a,b) &= \int_{\mathbb{R}^2} f(a+x,b+y)\overline{(\Lambda_\phi g)(x,y)}\,dx\,dy \\ &= \int_0^{2\pi}\int_0^{\infty} f^{(a,b)}(r,\beta)\overline{(\Lambda_\phi g)(r,\beta)}\,r\,dr\,d\beta \\ &= 2\pi\sum_m \Big(\int_0^{\infty} \big(\widehat{f^{(a,b)}}\big)_m(r)\overline{\hat{g}_m(r)}\,r\,dr\Big)\cdot e^{im\phi} \end{aligned} \tag{40}$$

from which we can read its Fourier transform:

$$\hat{c}(m;a,b) = 2\pi\int_0^A \big(\widehat{f^{(a,b)}}\big)_m(r)\overline{\hat{g}_m(r)}\,r\,dr \tag{41}$$

where A is the radius of the images. Thus, for each center (a, b) an inverse fast Fourier transform gives the correlation as a function of the angle ϕ.

We now describe a variation of this method, which essentially amounts to performing the angular sampling using a number of samples proportional to r. In this paper we call this variation "new RPC" in order to distinguish it from the standard way given by Eq. (41) ("old RPC"), although the idea of a variable angular sampling was already proposed[14] in order to avoid oversampling near the center. Here we do not actually vary the angular sampling step along r, but rather use a frequency-dependent integration interval.

According to the assumed bandwidth of the images, $\hat{f}_m(r) = 0$ for $|m| \geq B$ and for all r, in particular, for $r = A$. Therefore, we have $\hat{f}_m(r) = 0$ for $|m| \geq B_r$, where $B_r = (r/A)B$. Thus, in the integral in Eq. (41) we must have $r > (A/B)|m|$, hence:

$$\hat{c}(m;a,b) = 2\pi\int_{\frac{A}{B}|m|}^A \big(\widehat{f^{(a,b)}}\big)_m(r)\overline{\hat{g}_m(r)}\,r\,dr \tag{42}$$

2.4. FRM2D Revisited

In the FRM2D method[4] the search scheme consists in rotating both images, while translating one of them along the positive x-axis only. In this way there are two angles that are determined by Fourier transforms, while the translation is scanned. Thus, if ϕ, ϕ' are the angles and ρ is the translation distance, the correlation function is, according to Eq. (6) in Cong et al.:[4]

$$c(\phi,\phi';\rho) = \sum_{m,n} e^{i(m\phi+n\phi')} I_{mn}(\rho) \tag{43}$$

where

$$I_{mn}(\rho) = \hat{c}(m,n;\rho) = 2\pi\int_0^A \big(\widehat{h^n_{r,\rho}}\big)_m \cdot \overline{\hat{g}_m(r)}\cdot r\,dr \tag{44}$$

with

$$h^n_{r,\rho}(\beta) = e^{-in\beta'}\overline{\hat{f}_n(r')} \tag{45}$$

(We have interchanged f and g to match our present notation; refer to Cong et al.[4] for more details about this method). Then, for each ρ, an inverse 2D fast Fourier transform gives the correlation as a function of the angles ϕ and ϕ'.

Next we describe an improvement of this method. We observe that, since ρ is usually small compared to the radius A of the images, the distance r' will remain approximately equal to r for all β over most of the image, and the angle β' will likewise be close to β for most points. Therefore, the Fourier transform $(\widehat{h^n_{r,\rho}})_m$ will be small except for values of m such that $m+n$ is small. This tells us that the efficiency of the method can be increased by making the following change of indices and variables: $q = m+n$ and $\psi = \phi' - \phi$, for, then, the correlation becomes:

$$\begin{aligned} c(\phi,\phi';\rho) &= \sum_{q,n} e^{i[(q-n)\phi+n\phi']} I_{q-n,n}(\rho) \\ &= \sum_{q,n} e^{i(q\phi+n\psi)}\tilde{I}_{qn}(\rho) \\ &=: \tilde{c}(\phi,\psi;\rho) \end{aligned} \tag{46}$$

Hence, the Fourier transform of $\tilde{c}$ is

$$\begin{aligned} \hat{\tilde{c}}(q,n;\rho) &= \tilde{I}_{qn}(\rho) = I_{q-n,n}(\rho) \\ &= 2\pi\int_0^A \big(\widehat{h^n_{r,\rho}}\big)_{q-n}\cdot\overline{\hat{g}_{q-n}(r)}\cdot r\,dr \end{aligned} \tag{47}$$

Table I. Operation counts for the various real-space methods considered in this paper. Two numerical examples are given, corresponding to values 4 and 10 of the number of displacement samples k. The bandwidth B is half of the number s of angular samples of the images.

Method	N_{op}	$B=128, k=4$	$B=128, k=10$
$\text{FRM2D}^a_{\text{old}}$	$7.64B^3k+7.64B^3$	80,111,205	176,244,651
RPC'_{old}	$12B^2k^2+13.54B^2k$	4,033,085	21,879,193
RPC_{new}	$6B^2k^2+6.77B^2k$	2,016,543	10,939,596
$\text{FRM2D}_{\text{new}}$	$6B^2k^2+4.09B^2k$	1,840,906	10,500,506
FBM	$2.87B^2k^2-0.31B^2k$	732,037	4,651,418

[a]This method is of higher order of complexity than the others, unless $k \sim B$.

As in the RPC case, the assumed bandwidth of the images implies that $\hat{g}_m(r)=0$ for $|m| \geq (r/A)B$, and so we can restrict ourselves to $|q-n| < (B/A)r$. Similarly, from the definition of $h^n_{r,\rho}$ we get $|n| < (B/A)r'$, but since $r' \approx r$ almost everywhere, we have $|n| < (B/A)r$. We can write these two conditions in one as $r > r_0(q,n)$, where $r_0(q,n) = (A/B)\max\{|n|,|q-n|\}$. Thus, the Fourier transform of the correlation function becomes:

$$\hat{\tilde{c}}(q,n;\rho) = 2\pi \int_{r_0(q,n)}^{A} \left(\widehat{h^n_{r,\rho}}\right)_{q-n} \cdot \overline{\hat{g}_{q-n}(r)} \cdot r\,dr \quad (48)$$

2.5. Arithmetic Operation Counts

The operation counts for the correlation-based methods considered above are summarized in Table I. They are expressed as functions of the bandwidth B and the displacement parameter k. Also shown are two particular cases of values of B and k, which are displayed in Figures 5 and 6. Details of the derivation of these formulas are given in Appendix B.

It should be taken into account that all operation counts presented here refer to real multiplications, unlike those previously given in Ref. [4], which are complex multiplications. In addition, in order to make a comparison with the operation counts presented in that publication[4] possible, one should substitute $2s/\pi$ for their n (image size), since that is the number of samples on the diameter of the image (cf. Fig. 2). (The reader is advised that there seem to be some errors in the operation counts previously presented,[4] even after considering that they are counting complex multiplications rather than real ones, as we do here.)

A comparison of FBM with the SCF method is shown in Figure 7. Since SCF decouples the shift from the rotation, its operation count depends only on B. Hence, to compare it with FBM, we make k dependent on B through Eq. (26) combined with a relation between $\rho_{\max}$ and A according to the SNR values of the given images. Details are given in Appendix B.

We observe that the FBM curve corresponding to high SNR crosses the SCF curve at $B=137$, and the curve for low SNR crosses the SCF one at $B=65$. This means that even for cases in which it is safe to use the SCF method (i.e., high SNR), the FBM method can be used advantageously up to $B=137$, which corresponds to an angular sampling step of $\approx 1.3°$. And for cases of low

```
for(j=0,...,2B/pi-1){
  for(m1=-M[j],...,M[j]){
    c1 = J[m1,b*x[j]] * x[j]
    for(h1=-H[j],...,H[j]){
      c2 = J[h1,b*x[j]] * c1
      for(m'=0,...,m0[x[j]]){
        T_hat[m1,h1,m'] +=
          F[m1+h1+m',x[j]] * G[m',x[j]] * c2
      }
    }
  }
}
for(m1=-(pi*k/2-1),...,pi*k/2-1){
  for(h1=-(k/2-1),...,k/2-1){
    for(m'=0,...,B-1){
      T_hat[m1,h1,m'] *= tpe[h1+m']
    }
  }
}
```

Fig. 4. Pseudocode to show how $\widehat{T}$ is computed and to derive the operation count. `tpe`$[n]$ stands for $2\pi e^{in\epsilon}$. This, as well as $J_n(bx_j)$, $F_m(x_j)$, and $G_{m'}(x_j)$, are precomputed.

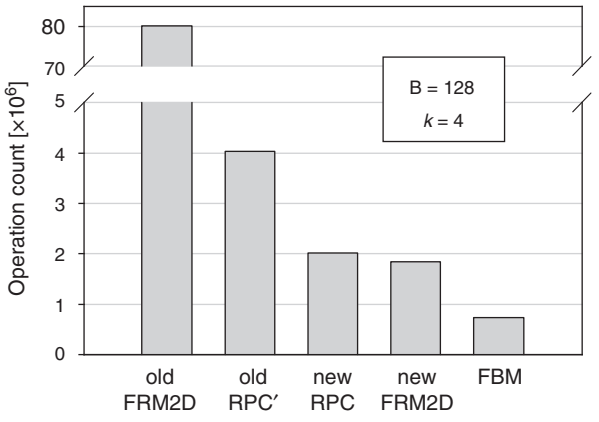

Fig. 5. Comparison of the operation counts of the various methods for bandwidth $B=128$ and displacement sampling $k=4$.

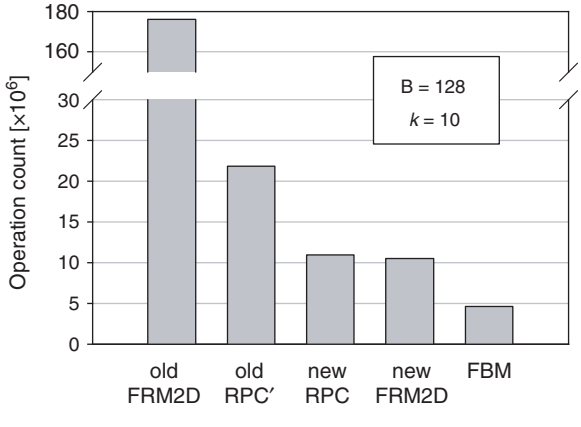

Fig. 6. Comparison of the operation counts of the various methods for bandwidth $B=128$ and displacement sampling $k=10$.

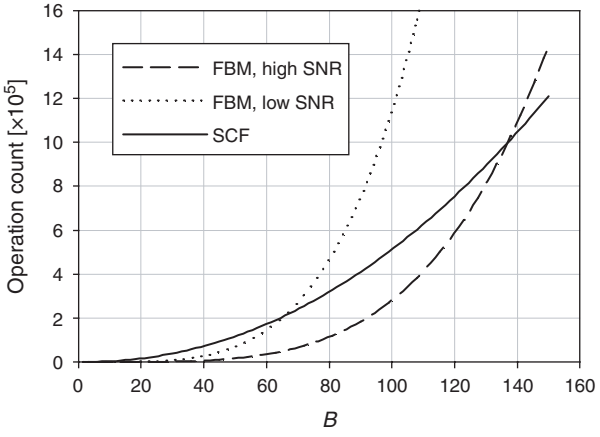

Fig. 7. Contrast between FBM and SCF. The latter method decouples the rotational and translational searches and is therefore of lower order of complexity than FBM. However, FBM has a better operation count up to $B = 65$ for cases of low SNR (where SCF cannot be used) and up to $B = 137$ for cases of high SNR. These plots correspond to Eqs. (64) and (66) (Appendix B.4).

SNR, FBM has an operation count of $\approx 3 \times 10^6$ for $B = 128$, while the value for SCF is $\approx 8.6 \times 10^5$, a ratio of only 3.5.

3. CONCLUSIONS

In this work, we present FBM, an efficient method to perform the image-matching step in the single-particle method of EM image reconstruction. This method is based on maximizing the correlation function between one of the images and a moved version of the other. This standard criterion underlies other methods as well, such as RPC and FRM2D. It is also at the base of 3D fitting algorithms,[18] although their contour-enhancement approach—which furnishes a significant contrast increase relative to the plain correlation method—cannot be applied in our case due to the relatively high noise level of the particle images. What we present here is a new approach to compute the correlation function, in such a way as to avoid sequentially scanning any of the parameters that define a rigid motion. We are able to achieve this by factorizing, in an adequate way, motions of the plane, and by combining this factorization with key properties of Bessel functions which allow us to directly obtain the Fourier transform of the correlation function with respect to a set of three angular variables. This expression involves the Fourier–Bessel transforms of the given images.

In this paper we have presented the theory of the method as well as a detailed description of the discretization of the formulas and the algorithm to do the actual implementation, from which we also calculated the operation count in terms of the sampling parameters. In addition, we described variations and improvements of the RPC and FRM2D methods, namely a way to effectively make the angular sampling radially dependent, and, for FRM2D, a change of parameters that brings it to the same level of complexity as RPC. We note that these features are already built in the FBM method. Even with these optimizations, FBM turned out to be more than twice as fast. This is due essentially to the presence of the Bessel-function factors in the integral (25), which implies the reduction of the m_1 and h_1 bandwidths according to Eq. (33). Also, FBM has less precomputation overhead, both in time and storage, since the Fourier–Bessel transform of an image is an array of nearly the same size as the original image. Instead, in the RPC and FRM2D methods, one has to compute, for each reference image, a set of transforms corresponding to the range of positions of the center of the moving (particle) image, of which there are about πk^2.

We also showed how FBM compares with the SCF method, which decouples the rotational and translational searches by means of dropping the phases of the Fourier transforms of the images. This entails a lower order of complexity than FBM and the other real-space methods, but at the cost of being more sensitive to noise.[4] Our comparison showed that FBM is competitive with SCF in regard to operation counts for a significant range of sampling parameters, being even more efficient than SCF up to bandwidths $B = 137$ for cases of high SNR, and is only 3.5 times slower than SCF for cases of low SNR (where SCF cannot be used) at $B = 128$.

A forthcoming publication will report applications of this method to actual image reconstructions. The use of our method will entail an important relief in large reconstructions involving images with low signal-to-noise ratios. In these cases, a correlation-based method must be used since others, including SCF,[5] are more sensitive to noise. Based on the timing comparisons presented here, we expect that FBM will be the method of choice in these cases.

Finally, we suggest that FBM might actually be the optimal real-space method for rigid-body matching of images, at least if we can neglect the precomputation overhead (Fourier–Bessel transforms). (This is certainly the case in EM image reconstruction since the number of matchings to be done is significantly larger than the number of images). We make this suggestion because is that the basis functions that appear in our formulas (products of exponentials and Bessel functions) are the matrix elements of the irreducible representations of the group of motions of the plane.[16] This makes the Fourier–Bessel transform the "natural" way to expand functions on the plane when they are going to be acted upon by elements of this group (rigid motions). A similar thing happens on the sphere,[7] where the basis functions are the spherical harmonics. In both cases, the basis functions have certain unique properties that allow a factorization of the motion (or rotation on the sphere) in such a way that the three parameters that define an element of the group can be collected in the exponential factor, thereby yielding an efficient expression for the Fourier transform of the correlation function. The naturality of the Fourier–Bessel transform for planar problems

has made its use very widespread in a variety of fields, but, as pointed out by Baldwin and Penczek,[13] this transform has not yet been fully taken advantage of in the EM image processing community. We hope that the present work will contribute to make a step forward in this regard.

Acknowledgments: We thank Yao Cong for stimulating discussions on earlier tentative approaches to the image-matching problem in EM reconstructions. We are also grateful to Irina Kufareva for carefully reading the manuscript. This work was supported by NIH grants 2 R01 HL048908-11 (M.Y.) and 1 R01 GM071872-01 (R.A.).

APPENDICES

A. Another Calculation of the x Bandwidth

Here we present a sketch of a more rigorous proof that the highest value of x to be used in our equations is B/A.

The idea is to project the image onto a sphere of a very large radius R, approximately centered at the north pole. Let α be the angle subtended by the image radius, so $\alpha = A/R$. Since there are $2B/\pi$ samples on the radius of the image, the number of samples on a half-circle (from the north pole to the south pole) is $s' := 2B/\alpha = 2RB/A$. According to Driscoll's sampling theorem for spherical functions[19] (Theorem 3), the image (more correctly, the sampling that we have of it), as a function on the sphere, can be written as a spherical harmonic expansion with $B' = s'/2 = RB/A$ harmonics:

$$f = \sum_{l=0}^{B'-1} \sum_{m=-l}^{l} \hat{f}_{lm} Y_{lm} \tag{49}$$

where the Y_{lm} are the spherical harmonic functions.

Next, by using various properties of Bessel functions, especially those concerning their relations with Legendre functions,[15,20] we can write the spherical harmonic coefficients and functions as follows (with equality holding as $R \to \infty$ and $l \to \infty$):

$$\hat{f}_{lm} \approx \frac{(-1)^m \sqrt{\pi(2l+1)}}{R^2} \int_0^A \hat{f}_m(u) J_m\left(\frac{ul}{R}\right) u\,du \tag{50}$$

$$Y_{lm}(\theta, \lambda) \approx (-1)^m e^{im\lambda} J_m(\theta l) \tag{51}$$

Substituting these expressions into Eq. (49), we get (looking at f again as a function on the plane, in polar coordinates):

$$f(r, \lambda) \approx \sum_{|m|<B} e^{im\lambda} \sum_{l=L_0}^{RB/A-1} \frac{2l+1}{2R} \left(\int_0^A \hat{f}_m(u) J_m\left(\frac{ul}{R}\right) u\,du \right) \times J_m\left(\frac{rl}{R}\right) \cdot \frac{1}{R} \tag{52}$$

where L_0 is a sufficiently large (but fixed) number, and $R \gg L_0$. Making the substitution $x = l/R$, we see that, as $R \to \infty$, this expression tends to

$$\sum_{|m|<B} e^{im\lambda} \int_0^{B/A} F_m(x) J_m(rx) x\,dx \tag{53}$$

with $F_m(x)$ being as in Eq. (10) except that the upper limit of the radial integral is now A. This expansion of f is as Eq. (13) with the upper limit of integration being now B/A and the summation over m being limited to B.

B. Operation Counts

Here we derive formulas for the number of elementary operations (products of real numbers) needed to carry out the matching of two images, for each of the methods considered in this paper.

B.1. FBM

For FBM, the matching of two images requires the evaluation of Eq. (25) for a range of index triplets (m_1, h_1, m'). Since the correlation function $T(\xi, \eta', \omega') = c(M)$ is real, we need only compute $\widehat{T}$ for $m' \geq 0$.

According to Eq. (36), the integral (25) is discretized using the lattice points $x_j = j\pi/(2A)$ with $j = 0, 1, \ldots, (2B/\pi) - 1$. (Notice that $j = 2B/\pi$ gives $x_j = B/A$, for which the Fourier–Bessel transforms inside the integral vanish due to the assumed bandwidth).

Hence, for $x = x_j$, m' will vary from 0 to $m_0(x_j)$. As to m_1 and h_1, they will vary from $-M_j$ to M_j and from $-H_j$ to H_j, respectively, where, due to Eqs. (30), (31), and (33),

$$M_j = \min\left\{ \frac{ebx_j}{2}, \frac{2Bb}{A} - 1 \right\} \tag{54}$$

$$H_j = \min\left\{ \frac{ebx_j}{2}, \frac{2Bb}{\pi A} - 1 \right\} \tag{55}$$

Now, as pointed out earlier, the way we compute $\widehat{T}$ is by taking each of the x_js and computing the integrand for the corresponding ranges of indices, adding the terms to the corresponding entries of the $\widehat{T}$ array. Thus, the number of operations (real multiplications) needed for the evaluation of $\widehat{T}$ is, according to the pseudocode in Figure 4:

$$\sum_{j=0}^{\frac{2B}{\pi}-1} \left\{ (2M_j+1)[1+(2H_j+1)[1+6(m_0(x_j)+1)]] \right\} + 4\pi Bk^2 \tag{56}$$

When evaluating the operation count, we will only keep terms of order B^2k^2 and B^2k. Note that the quantities $J_n(bx_j)$ are to be precomputed for $|n| < \pi k/2$ and $j = 0, 1, \ldots, (2B/\pi) - 1$. Likewise, the Fourier–Bessel transforms $F_m(x_j)$ and $G_{m'}(x_j)$ are to be precomputed for all the reference and particle images to be matched. The precomputation of these transforms can be done with complexity $(N_r + N_p)B^2 \log B$ using fast methods,[21] where N_r

is the number of reference images and N_p that of particle images. Regardless of this, we assume that $N_r N_p$ is large compared to $N_r + N_p$, so the precomputation time is, in any event, negligible compared to the matching time, and thus it will not be included in the operation count. Likewise, the inverse fast Fourier transform, needed after $\widehat{T}$ has been computed, has complexity $Bk^2 \log(Bk^2)$, hence it too will be omitted from the operation count.

Now, in order to evaluate Eq. (56), let us call j_1 and j_2 the values of j where the crossing points in Eqs. (55) and (54), respectively, occur, i.e., such that

$$\frac{eb\pi j_1}{4A} = \frac{2Bb}{\pi A} - 1 \quad \text{and} \quad \frac{eb\pi j_2}{4A} = \frac{2Bb}{A} - 1 \tag{57}$$

These are given by:

$$j_1 = \frac{8B}{e\pi^2}\left(1 - \frac{2}{k}\right) \quad \text{and} \quad j_2 = \frac{8B}{e\pi^2}\left(\pi - \frac{2}{k}\right) \tag{58}$$

Accordingly, we need to distinguish three cases:

(1) $\frac{2B}{\pi} - 1 \le j_1$.

(2) $j_1 < \frac{2B}{\pi} - 1 \le j_2$.

(3) $j_2 < \frac{2B}{\pi} - 1$.

Case (1) implies $B(0.3384 + 0.596/k) \le 1$, hence $B < 3$, which does not occur in practice. Case (3) implies $k < 0.596B/(1 + 0.9368B)$, which is <0.636, so this case is also discarded. Hence, we consider only Case (2) for the computation of Eq. (56), splitting the summation at j_1. After substituting numerical values for e and π, we arrive at the following formula for the total number of operations needed to perform one matching:

$$N_{\text{op}} = 2.87B^2k^2 - 0.31B^2k + \text{lower-order terms} \tag{59}$$

B.2. RPC

The way to use the RPC method would be to compute, for each reference image f, the transforms $(\widehat{f^{(a,b)}})_m(r)$, store them in memory, and do the matching with each of the particle images g. In this way, the computation of these transforms can be neglected if we have a large number of particle images, as we are assuming. This is actually different from the original description of the RPC method,[2,14] which performs the above operations "on-the-fly." Hence, here we use a prime ($'$) to refer to the precomputed version of the original RPC method: "old RPC$'$." Also, the inverse FFTs will be neglected since they add only terms of lower order than those we keep. We are going to estimate the operation counts for both the "old" (Eq. (41)) and the "new" (Eq. (42)) RPC methods under these conditions.

Before going into the two cases, let us determine the number l of centers (a, b) to be explored. For this, we note that the increments in a and b should be equal to p_s, and since the maximum translation of the moving image is $\rho_{\max} = 2b$, the area to be explored is $\pi\rho_{\max}^2$. Therefore, there are approximately $N_s = \pi\rho_{\max}^2/p_s^2 = \pi k^2$ squares of side p_s in the circle of radius $\rho_{\max}$. It is easy to see that the number of vertices of these squares is $l = (\sqrt{N_s} + 1)^2 = (\sqrt{\pi}k + 1)^2 = \pi k^2 + 2\sqrt{\pi}k + 1$.

Old RPC$'$. Since the Fourier transforms are computed for $2B/\pi$ radial values, the integral in Eq. (41) will also be discretized using this number of intervals, and since the images are real-valued functions, we need to compute $\hat{c}$ only for $m \ge 0$, that is, for B values of m. Therefore, the number of integrand evaluations, for each center (a, b), is $2B^2/\pi$. The number of multiplications for each integrand evaluation is 6, because $\hat{f}$ and $\hat{g}$ are complex. Hence, the total number of operations is:

$$N_{\text{op}} = \frac{2B^2}{\pi} \cdot 6 \cdot l = \frac{12}{\pi}B^2 l \approx 12B^2k^2 + 13.54B^2k \tag{60}$$

New RPC. In this case, the number of integration intervals (Eq. (42)) is $(2/\pi)(B - |m|)$, and, as before, we need only consider $m \ge 0$. The number of integrand evaluations, for all m and for each center, is now $\sum_{m=0}^{B-1}(2/\pi)(B-m) = B(B+1)/\pi$, and the total number of operations is:

$$N_{\text{op}} = \frac{B(B+1)}{\pi} \cdot 6 \cdot l \approx \frac{6}{\pi}B^2 l \approx 6B^2k^2 + 6.77B^2k \tag{61}$$

which is half of that of the old RPC$'$ method.

B.3. FRM2D

The way to use the FRM2D method would be to compute, for each reference image f, the transforms $(\widehat{h^n_{r,\rho}})_m$, store them in memory, and do the matching with each of the particle images g. In this way, the computation of these transforms can be neglected if we have a large number of particle images, as we are assuming. Also, the inverse FFTs will be neglected since they add only terms of lower order than those we keep. We are going to estimate the operation counts for both the "old" FRM2D (Eq. (44)) and the new version (Eq. (48)), under these conditions.

Before going into the two cases, let us determine the number of sampling points for ρ and the bandwidth for q in the new version. (In the old version, both m and n have bandwidth B.) Since the increment in ρ should be p_s, the number of sampling points for ρ is $\rho_{\max}/p_s + 1 = k + 1$.

Since q is the coefficient of ϕ in $\tilde{c}$, the bandwidth for q (or ϕ) is $B_\phi = (1/2)2\pi/\Delta\phi$, where the angular step $\Delta\phi$ should satisfy $2p_s = \rho_{\max}\Delta\phi$. Therefore $B_\phi = \pi k/2$. The bandwidth for n (or ψ) remains B. We remark here that the change from the m of the old FRM2D to the q of the new version allows, as shown below, an important complexity reduction, since the bandwidth of m is B (it cannot be

taken of the order of k because m must always be close to n, which has bandwidth B), while the bandwidth of q is $\pi k/2$.

Old FRM2D. Since the Fourier transforms are computed for $2B/\pi$ radial values, the integral in Eq. (44) will also be discretized using this number of intervals, and since the images are real-valued functions, we need to compute $\hat{c}$ only for $n \geq 0$, that is, for B values of n. The index m will range over the whole interval: $-B < m < B$. Therefore, the number of integrand evaluations, for each m, each ρ and all n, is $2B^2/\pi$. The number of multiplications for each integrand evaluation is 6, because $\hat{h}$ and $\hat{g}$ are complex. Hence, the total number of operations is:

$$\begin{aligned} N_{\text{op}} &= \frac{2B^2}{\pi} \cdot 6 \cdot (2B-1) \cdot (k+1) \\ &= \frac{12}{\pi} B^2 (2B-1)(k+1) \\ &\approx 7.64B^3 k + 7.64B^3 \end{aligned} \tag{62}$$

We note that this method has a higher order of complexity than the others, and thus is better than the old RPC′ method only when k is comparable to B. FRM2D compared favorably[4] to the old RPC method because, in that publication, the operation count for the RPC method was computed under the assumption that the resampling to polar coordinates and the corresponding 1D FFTs of the reference images are carried out "on the fly,"[2] rather than being precomputed as we do here.

New FRM2D. In this case, the number of integration intervals (Eq. (48)) is approximately $(2/\pi)(B-|n|)$ (disregarding the influence of q since it is small), and, as before, we need only consider $n \geq 0$. The index q will range over the interval $-\pi k/2 < q < \pi k/2$. The number of integrand evaluations, for each q, each ρ and all n, is now $\sum_{n=0}^{B-1} (2/\pi)(B-n) = B(B+1)/\pi$, and the total number of operations is:

$$\begin{aligned} N_{\text{op}} &= \frac{6}{\pi} B(B+1)(\pi k - 1)(k+1) \\ &\approx 6B^2k^2 + 4.09B^2 k \end{aligned} \tag{63}$$

B.4. SCF

Here we compute the operation count of the SCF method in terms of our sampling parameters and see how it compares with FBM. Details on the SCF method have been presented elsewhere.[2] We assume, as usual, that the FFTs and SCFs of the given images are precomputed.

(1) The first step is to get the rotation angle of the particle image, and this can be done by using the "new RPC" method applied to the SCFs, but without exploring shifts. This step needs therefore $(6/\pi)B^2$ operations.

(2) For the angle found, and for the angle plus 180°, we have to:

(a) Rotate the particle image and compute its FFT. In theory, and to avoid performing an extra FFT, this can be done in a single step by rotating the Fourier transform of the original image, which, due to symmetry, can be taken as an $(s/\pi) \times (2s/\pi)$ (complex) array. Therefore, its rotation takes $12 \cdot 2s^2/\pi^2 = (96/\pi^2)B^2$ operations, since 12 real multiplications per point are needed to perform the rotation of a complex-valued image using bilinear interpolation.

(b) Compute the Fourier transform of the correlation function as the product of the Fourier transforms of the reference projection and of the rotated particle. Since these are complex-valued, each product takes 4 real multiplies, hence this step takes $32B^2/\pi^2$ operations.

(c) Compute the inverse FFT to get the correlation function and thereby the translation. The most efficient practical algorithm for the FFT known to date is the "split-radix FFT," which, for real data whose length N is a power of 2, needs $(2/3)N \log_2 N - (19/9)N$ real multiplies.[22] With $N = (2s/\pi)^2$ this is $(64/3\pi^2)B^2 \log_2 B + (192 \log_2(4/\pi) - 304)/(9\pi^2)B^2$ operations.

Therefore, the total number of operations for one matching is:

$$\begin{aligned} N_{\text{op}} &= \frac{128}{3\pi^2} B^2 \log_2 B + \frac{2464 + 54\pi - 384 \log_2 \pi}{9\pi^2} B^2 \\ &\approx 4.323B^2 \log_2 B + 22.51B^2 \end{aligned} \tag{64}$$

Comparison with FBM. As mentioned earlier, the value of $\rho_{\max}$ depends on the quality of the images. For high-SNR images, we use $\rho_{\max} = A/20$, where A is the radius of the images, whereas for low SNR we use $\rho_{\max} = A/10$. Therefore,

$$\begin{aligned} k = \frac{\rho_{\max}}{p_s} &= \begin{cases} \dfrac{A}{20p_s} = \dfrac{B}{10\pi} & \text{for high SNR} \\ \dfrac{A}{10p_s} = \dfrac{B}{5\pi} & \text{for low SNR} \end{cases} \\ &= \gamma B \end{aligned} \tag{65}$$

so that $\gamma = (10\pi)^{-1}$ for high SNR and $\gamma = (5\pi)^{-1}$ for low SNR. Then, the FBM operation count, Eq. (59), becomes

$$N_{\text{op}} = (2.87\gamma B - 0.31)\gamma B^3 \tag{66}$$

Eqs. (64) and (66) (for the two values of γ just given) are plotted in Figure 7.

References

1. J. Ruprecht and J. Nield, *Prog. Biophys. Mol. Biol.* 75, 121 (**2001**).
2. L. Joyeux and P. A. Penczek, *Ultramicroscopy* 92, 33 (**2002**).
3. R. M. Glaeser, *J. Struct. Biol.* 128, 3 (**1999**).
4. Y. Cong, J. A. Kovacs, and W. Wriggers, *J. Struct. Biol.* 144, 51 (**2003**).
5. M. Schatz and M. van Heel, *Ultramicroscopy* 45, 15 (**1992**).
6. M. van Heel, M. Schatz, and E. Orlova, *Ultramicroscopy* 46, 307 (**1992**).
7. J. A. Kovacs and W. Wriggers, *Acta Cryst. D* 58, 1282 (**2002**).

8. S. J. Ludtke, P. R. Baldwin, and W. Chiu, *J. Struct. Biol.* 128, 82 **(1999)**.
9. J. Navaza, *J. Struct. Biol.* 144, 13 **(2003)**.
10. S. Darst, N. Opalka, P. Chacón, A. Polyakov, C. Richter, G. Zhang, and W. Wriggers, *Proc. Natl. Acad. Sci. USA* 99, 4296 **(2002)**.
11. J. G. Mandell, V. A. Roberts, M. E. Pique, V. Kotlovyi, J. C. Mitchell, E. Nelson, T. Tsigelny, and L. F. T. Eyck, *Protein Engineering* 14, 105 **(2001)**.
12. H.-W. Wang and E. Nogales, *J. Struct. Biol.* 149, 65 **(2005)**.
13. P. R. Baldwin and P. A. Penczek, *J. Struct. Biol.* 150, 211 **(2005)**.
14. P. Penczek, M. Radermacher, and J. Frank, *Ultramicroscopy* 40, 33 **(1992)**.
15. G. N. Watson, A Treatise on the Theory of Bessel Functions, Cambridge Mathematical Library, Cambridge University Press, Cambridge, UK **(1996)**.
16. N. J. Vilenkin, Special functions and the theory of group representations. Translations of Mathematical Monographs, American Mathematical Society, Providence, Rhode Island **(1968)**, No. 22.
17. M. Abramowitz and I. A. Stegun (eds.), Handbook of Mathematical Functions, Dover, New York **(1972)**.
18. P. Chacón and W. Wriggers, *J. Mol. Biol.* 317, 375 **(2002)**.
19. J. R. Driscoll and D. M. Healy, Jr., *Advances in Applied Mathematics* 15, 202 **(1994)**.
20. D. A. Varshalovich, A. N. Moskalev, and V. K. Khersonskii, Quantum Theory of Angular Momentum, World Scientific **(1988)**.
21. S. Candel, *IEEE Transactions on Acoustics, Speech, and Signal Processing* 29, 963 **(1981)**.
22. H. V. Sorensen, M. T. Heideman, and C. S. Burrus, *IEEE Trans. Acoust. Speech, Signal Processing* 34, 152 **(1986)**.

Received: 26 May 2006. Accepted: 11 July 2006.